Supplementary Materials for

Biogel scavenging slows the sinking of organic particles to the ocean depths

Uria Alcolombri[1,*], Alon Nissan[2], Jonasz Słomka[3], Sam Charlton[3], Eleonora Secchi[3], Isobel Short[3], Kang Soo Lee[4], François J. Peaudecerf[5], Dieter Baumgartner[3], Andreas Sichert[6], Uwe Sauer[6], Anupam Sengupta[7,8] and Roman Stocker[3,*]

[1] Institute for Life Sciences, Department of Plant and Environmental Sciences, The Hebrew University of Jerusalem, Jerusalem, Israel.

[2] The Robert H. Smith, Faculty of Agriculture, Food and Environment. Department of Soil and Water Sciences. The Hebrew University of Jerusalem, Rehovot, Israel.

[3] Institute of Environmental Engineering, Department of Civil, Environmental and Geomatic Engineering, ETH Zurich, Zurich, Switzerland.

[4] Department of Mechanical Engineering, Ulsan National Institute of Science and Technology (UNIST), Ulsan 44919, South Korea

[5] Univ Rennes, CNRS, IPR (Institut de Physique de Rennes) - UMR 6251, F-35000 Rennes, France.

[6] Institute of Molecular Systems Biology, Department of Biology, ETH Zurich, Zurich, Switzerland.

[7] Physics of Living Matter Group, Department of Physics and Materials Science, University of Luxembourg, 162 A, Avenue de la Faïencerie, L-1511 Luxembourg City, Luxembourg.

[8] Institute for Advanced Studies, University of Luxembourg, 2 Avenue de l'Université, L-4365 Esch-sur-Alzette, Luxembourg.

*Corresponding authors. Email: Uria.Alcolombri@mail.huji.ac.il (U.A), romanstocker@ethz.ch (R.S).

The PDF file includes:

Supplementary Methods
Supplementary Text
Fig. 1 to 14
References

Other Supplementary Materials for this manuscript include the following:

Movies 1 to 6
Table S1
Data S1

Supplementary Methods

Mathematical Model

3D-numerical modeling to study the effect of biofilm accumulation on particles

A three-dimensional (3D) numerical model was developed to study the effect of biofilm accumulation on particle sinking speed and to disentangle the effects of changes in density and hydrodynamic drag caused by biofilm accumulation. The model couples fluid flow simulations with an ordinary differential equation (ODE) to calculate the balance of forces that act on a solid object while sinking. The fluid flow within the 3D domain is described by the Navier–Stokes equations,

(Eq. 1)

$$\rho\frac{\partial u}{\partial t} - \nabla\cdot\eta(\nabla u + (\nabla u)^T) + \rho u\cdot\nabla u + \nabla p = F_z$$

$$\nabla\cdot u = 0,$$

where ρ is the particle density (kg m^{-3}), u is the velocity vector (m s^{-1}), η is the fluid viscosity (10^{-3} Pa s), and p is the pressure field (Pa). The model uses the accelerating reference system of the particle. This means that the volume force density F_z is given by

(Eq. 2)

$$F_z = -\rho_f(a+g),$$

where ρ_f is the fluid density (here taken for simplicity as 1000 kg m^{-3}), where a (m s^{-2}) is the acceleration of the solid object, and g = 9.81 m s^{-2} is the gravitational acceleration. The ODE that describes the balance of forces is

(Eq. 3)

$$\frac{dv_s}{dt} = \frac{F_d + F_g}{m},$$

where v_s (m s^{-1}) is the sinking velocity, m is the mass (kg) of the particle, F_d represents the total force exerted by the fluid on the particle, computed by integrating the total stress—comprising pressure and viscous stresses—over the particle's surface in the direction of the flow. F_g is the gravitational force, given by

(Eq. 4)

$$F_g = -\rho_s V_s g,$$

with ρ_s the density (kg m^{-3}) and V_s the volume (m^3) of the particle. At the lower face (inlet) of the domain, the boundary condition is equal to the sinking velocity (v_s). Note that we did not account for particle rotation, as no significant rotation was observed during the experiments; thus, the particle's initial orientation was kept constant throughout the simulation. An open boundary condition, $\frac{\partial u}{\partial n} = 0$ (where n is the normal vector) was applied at the upper boundary to allow the fluid to exit the computational domain freely. The boundary surfaces oriented along the z-axis are subjected to a slip boundary condition. Specifically, the tangential velocity at these boundaries is directly proportional to the corresponding shear rate.

The system of equations consists of the Navier-Stokes equations coupled with an ordinary differential equation (ODE) to compute the balance of forces acting on the particle, including gravitational and drag forces. The equations were solved using the LiveLink MATLAB-COMSOL interface, with MATLAB responsible for problem parameterization and execution of two COMSOL models—one for creating the particle geometry and another for performing the sinking speed simulation. The model workflow is illustrated in Supplementary Fig. 14. The process begins in MATLAB, where key problem parameters are defined, including fluid properties such as density and viscosity, particle characteristics such as size and density, and the number, orientation, length, and radius of the hydrogel tendrils. These parameters are then automatically transferred to COMSOL, where the composite object, consisting of the particle and tendrils, is generated and meshed. Due to the discretization inherent in the computational mesh, the resulting composite object may exhibit slight deviations from the analytically specified properties in MATLAB. Consequently, key properties such as mass, density, and volume within COMSOL are recalculated at that stage in order to ensure accurate characterization for subsequent analysis. The meshed composite object, with its recalculated properties, is then passed back to MATLAB and subsequently used to execute the second COMSOL model to calculate the sinking velocity (through solution of Equations 1–4). An iterative solver in COMSOL ensures the convergence of the ODE, with the simulation concluding once the particle reaches its terminal velocity.

Throughout the simulation, we observed the change in the sinking speed of the particle (v_s) at low Reynolds numbers (Re << 1), beginning from a stationary state (i.e., v_s = 0) until an asymptotic steady-state condition was attained (i.e., terminal velocity was achieved; see Supplementary Fig. 14). Specifically, the numerical solver iterates over the ODE (Eq. 3), computes the balance of

forces and determines the corresponding v_s. Subsequently, in the next iteration, the inlet boundary condition is updated to v_s. Our starting point involves a spherical particle with a density ρ_s = 1100 kg m^{-3} and a radius $R_0 = 2.5 \times 10^{-4}$ m to simulate typical particle characteristics [1–3]. Next, to study the experimental findings—specifically, the decrease in sinking speed due to biofilm attachment—we attach eight tendrils with a density ρ_b to the particle's perimeter at a 45° angle to the z-axis. This addition increases both the particle's mass and surface area. By adjusting the tendrils' length (ℓ_t), we analyze how the particle's surface area and mass influence the drag and, consequently, the sinking speed. For simplicity, we assume tendrils with a fixed thickness r_t (set to 0.1 R_0) and model the particle as a solid object with a no-slip boundary condition and no porosity.

For the purpose of this model, we consider two types of biogel that differ in their bulk density ρ_b

(i) Attachment of suspended biofilm with a density equivalent to that **of the water** ($\rho_\mathrm{b} = \rho_\mathrm{f}$), similar to the case of *A. macleodii* biofilm. In this case, elongation of the tendrils results in particles with increased mass and surface area but lower overall density.

(ii) Attachment of biofilm with a density equivalent to that **of the particle** ($\rho_\mathrm{b} = \rho_\mathrm{s}$). In this case, elongation of the tendrils results in particles with increased surface area, but with constant overall density.

In each simulation, the terminal velocity of the particle (v) is correlated with four key variables: particle mass (m), volume (V_s), density (ρ_s), and surface area (Ω). Our results are expressed using dimensionless numbers, with the variables scaled as follows: $m^* = \frac{m}{m_0}$, $\rho^* = \frac{\rho_\mathrm{s}}{\rho_{\mathrm{s}0}}$, $\Omega^* = \frac{\Omega}{\Omega_0}$, $V^* = \frac{V}{V_0}$, and $v^* = \frac{v}{v_0}$, where m_0, V_0 $\rho_{\mathrm{s}0}$, Ω_0 and v_0 are the particle's initial mass, volume, density, surface area, and terminal velocity, respectively (**Fig. 2, Supplementary Fig. 10**). The model was validated against the analytical solution of Stokes' Law by solving Eqs. 1–4 for a purely spherical particle. Note that the robustness of our model was also tested by performing a sensitivity analysis for all set parameters, including the number of tendrils (1–10), their angle relative to the particle (25°–85°), length (0.08-2.5 R_0) and their thickness (0.5–2 r_t) (**Supplementary Fig. 10).** This analysis revealed a minor effect of any simulation run with more than 3 tendrils and very little

effect of the angle of the tendrils and their thickness on the sinking of the particle, with a major effect of tendril elongation.

To estimate the predicted reduction in sinking speed in the environment, the relation between sinking speed v^* and particle volume (V^*) that were found in our numerical model (scenario (i)) were used to fit a linear curve and obtain the relation between the two parameters:

(Eq. 5)

$$v^* = -2.4 * V^* + 3.4 \quad (R^2 = 0.99).$$

Using this relation (Eq. 5), and calculating the relative volume of biogels that was accumulated on the surface of the particle in 100 m of depth (assuming all biogels stick upon encounter), we estimated the predicted reduction in sinking speed in the environment in response to different biogel concentrations and sizes in the water column (**Fig. 3D, Supplementary Fig. 11**).

Supplementary Text

***A. macleodii* and other heterotrophic biofilm-forming bacteria are relevant model systems for testing the effect of biogel on particles.**

The biofilm aggregates formed by *A. macleodii* serve as a good model system for the effect of biogel accumulation on particles. Suspended polysaccharides such as TEP and EPS are often heavily colonized by microorganisms, effectively functioning as suspended biofilms in the ocean [4,5]. Similar to many other marine biogels, *A. macleodii* biofilm aggregates are shown by our experiments to be sticky and attached to a variety of surfaces, including on glass surfaces and copepod fecal pellets (**Supplementary Fig. 5, Supplementary Movie 3**). Recent work by *Chajwa* and coworkers ([6]) shows how "invisible" mucous trails can alter particle sinking speeds. In contrast, in our system the biogels produced by *A. macleodii* are fully visible in phase microscopy (or with Alcian Blue staining; **Supplementary Fig 4**), with no hidden components (**Supplementary Fig. 5, Supplementary Movie 5**). This approach allowed us to closely track

particle dynamics that might be more challenging to observe in the presence of the diverse array of biogels in the ocean. Using a particle trapped in a microfluidic chamber under flow of ASW, we found that biofilm aggregates that accumulated on particles also promoted the attachment of free-swimming bacteria (*Marinobacter adhaerens* HP15) co-incubated with *A. macleodii*, further demonstrating their sticky nature (**Supplementary Fig. 5, Supplementary Movie 5**). Overall, the extensive accumulation of *A. macleodii* biofilm aggregates on several surface types suggests this process is likely to be widespread in environments where *A. macleodii* and other EPS-producing microorganisms are prevalent [7].

Besides the ability of *A. macleodii* to serve as a good biogel model, *A. macleodii* is commonly found in blooms of oceanic algae and, by forming biofilms and attaching to particles, has the potential to influence the fate of the carbon sequestered. Moreover, similar to the biofilm of *A. macleodii,* other bacterial species commonly found on marine snow, such as *Pseudomonas, Marinobacter,* and *Alcanivorax*, have been shown to produce thick biofilm on rising marine oil droplets while increasing the drag force that acts on them [8–10]. The formation of these suspended biofilm structures is favored by the viscoelastic nature of the biofilm matrix [11]. Once the matrix accumulates on a surface, the shear forces exerted by the flow promote its fluidization and extrusion into the bulk of the flow[12–15]. Additionally, bacterial cells and aggregates present in the surrounding fluid are captured by these suspended biofilms, leading to their rapid growth [16,17].

To understand the genetic makeup that allows the biogel formation by *A. macleodii,* we further characterized the biofilm composition and identified the genes responsible for EPS formation. Biofilm aggregates were chemically analyzed, and a bioinformatic survey of the *A. macleodii* genome was performed. Based on a bioinformatic analysis and literature survey, we propose several candidate loci responsible for the production of EPS by *A. macleodii* (Table S1). Similar to other biogels (e.g., TEP), *A. macleodii* biofilm aggregates were found to stain positively with Alcian blue, propidium iodine, and Coomassie blue, indicating the presence of polysaccharides and possibly eDNA and proteins, respectively (**Supplementary Fig. 4**). Additionally, while this work was in progress, a UDP-glucose-4-epimerase gene has been found to be essential for the formation of biofilm in *A. macleodii ATCC 27126* strain[18]. By analyzing the chemical composition of the biofilm aggregates using an acid-based polysaccharide fragmentation analysis

coupled with mass spectrometry, we found that the biofilm of *A. macleodii*, similar to other species of *Alteromonas* (e.g., ref [19]), is composed of a polymer containing glucose, glucuronic acid, mannose and other carbohydrates in varying ratios (**Supplementary Fig. 4**). Acidic sugars may provide the EPS of *A. macleodii* its viscoelastic, gel-like consistency, similar to xanthan gum, another polysaccharide with gel-forming properties that is also rich in glucuronic acid [20]). Overall, these results show that *A. macleodii*'s biofilm displays similar chemical and biophysical properties to other marine biogels, suggesting a possible unexplored role for *A. macleodii* and other marine bacteria in determining the fate of carbon in the ocean.

Heterotrophic bacteria may contribute to the biogel standing stock

To test the potential contribution of heterotrophic bacteria to the slowdown of particles by accumulating biofilm, we estimated the abundance and diversity of biofilm-forming bacteria on particles. To do so, we tested the prevalence of biofilm formation among 96 heterotrophic bacteria isolated from particles collected from the coast of Massachusetts, USA [21]. When cultured for two days in a rich medium (MB2216, 200 RPM), ~33% of the 96 isolates formed a biofilm, and in one-third of these cases, the biofilm was considerably thick and covered large part of the well (**Supplementary Fig. 8; Supplementary Materials and Methods**). Altogether, this suggests that biofilm formation may be widespread among heterotrophic bacteria in the ocean, possibly as it increases the chances of encountering through direct interception and sticking to a nutrient-rich sinking particle. However, despite the high prevalence of biofilm-forming bacteria found on particles, not all biofilm-forming bacteria are able to form biofilm rigid enough to slow a sinking particle.

The biofilm buildup on particles in our experiment is mainly caused by biogel interception with the particle rather than bacterial growth

The rapid accumulation of biofilm on particles in our experiments was mostly a result of interception of the biofilm aggregates by the particles as they sank rather than biofilm production and growth by bacteria residing on the particles. This conclusion is based on microscopy experiments with single particles held in place in a microfluidic channel and exposed to a flow of artificial seawater containing *A. macleodii* biofilm (**Supplementary Materials and Methods**). Using the same experimental conditions as in our endless-ocean-column experiments and a similar flow speed, we observed that biofilm accumulation on the surface of the particle due to

interception was more prominent than bacterial growth **(Supplementary Movie 3)**. Furthermore, biofilm elongation occurred at the periphery of the particle as expected by interception, and swelling of the biofilm, which is expected with growth, was minor. During both experiments (the microfluidics and the endless-ocean-column), the particle's overall structure did not shrink or fragment as expected during degradation. Instead, there was a notable addition of biofilm, supporting the notion that, at least in our experimental setup, biofilm formation is the dominant reason for the observed slowdown. To further disentangle the effect of growth and degradation from the effect of biofilm interception, in a further experiment, a particle pre-colonized with *A. macleodii* (diluted 1:100 with stationary grown *A. macleodii* and incubated in a rolling tube for 1 h) was loaded and observed while sinking in the endless-ocean-column in sterile ASW (i.e., no further biofilm interception occurred, only growth on the particle). In this experiment, little biofilm growth was observed, and the reduction in particle sinking speed of 12% over 44 h (i.e., 0.27% h^{-1}) was smaller than the 30–45% reduction measured in the presence of a flowing suspension of biofilm aggregates over a period of 24 h (i.e., 1.25–1.8% h^{-1}) (**Supplementary Fig. 12, Supplementary Movie 6** compared with **Fig. 1B and Supplementary Movie 1**).

While encounter was the predominant mechanism of biofilm accumulation on particles in our experiment, we propose that the lability of particles in the environment is likely to vary [1,3], and consequently, biofilm encounters, biofilm growth, and particle degradation or disaggregation may all contribute to reducing the sinking speed. These additional mechanisms were not prominent in our specific experimental system but are likely to play a role in the environment, reinforcing our conclusion that biofilms and other biogels can interact with marine particles in different ways and, therefore, can change their sinking substantially based on the specific dominant mechanisms in action.

Supplementary figures

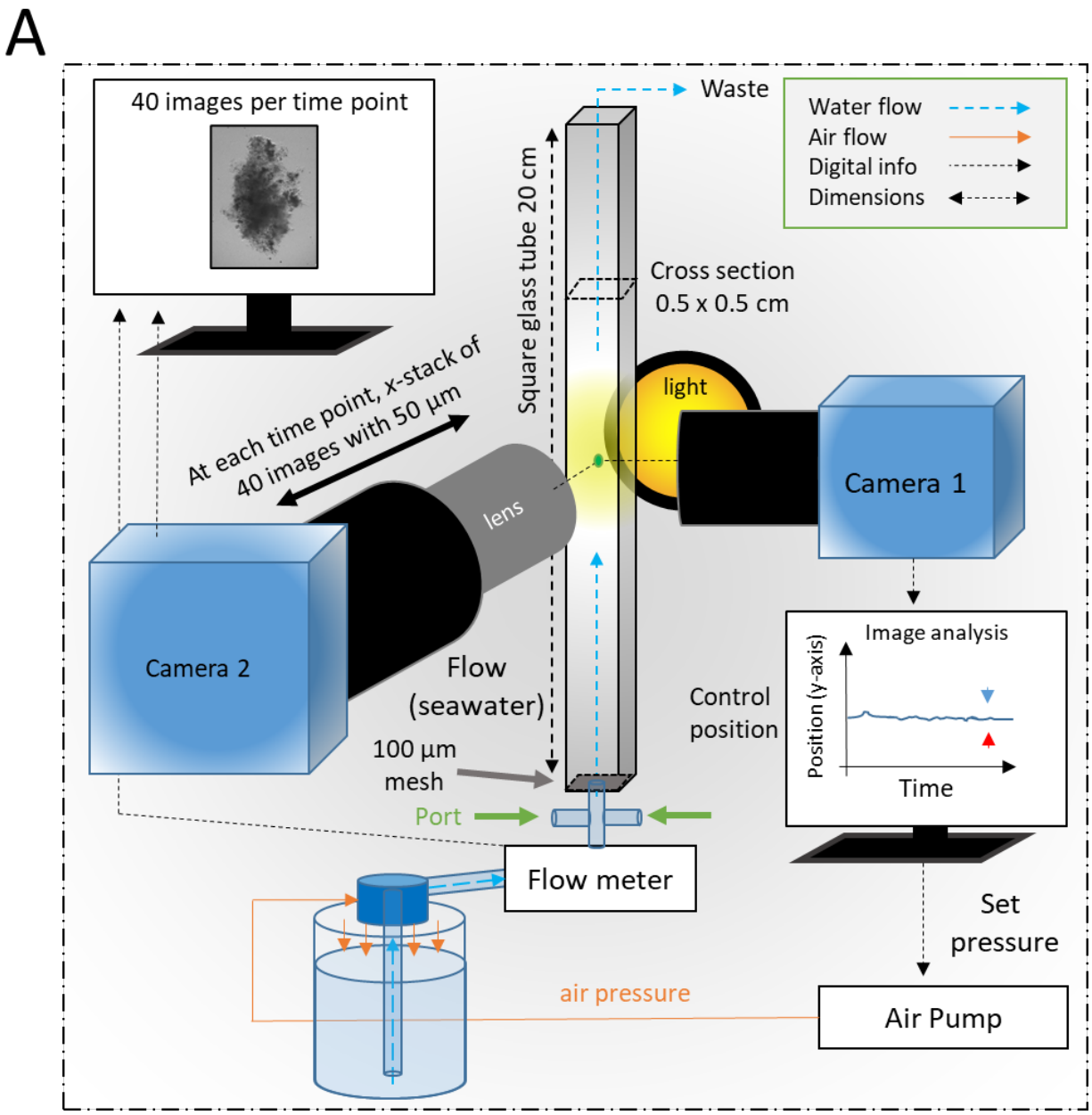

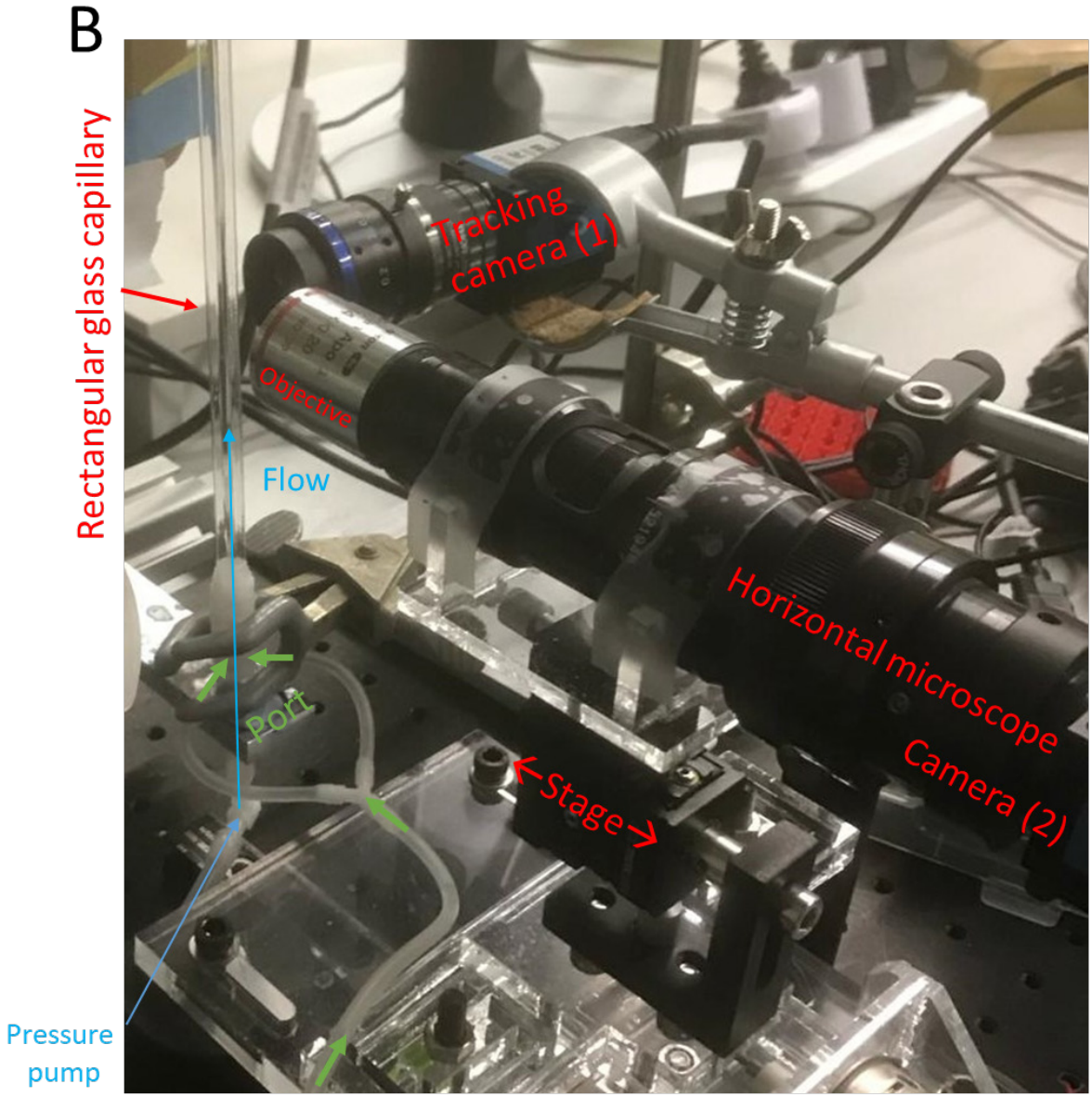

Syringe pump (active just when trapping the particle at the beginning of the experiment)

260
261

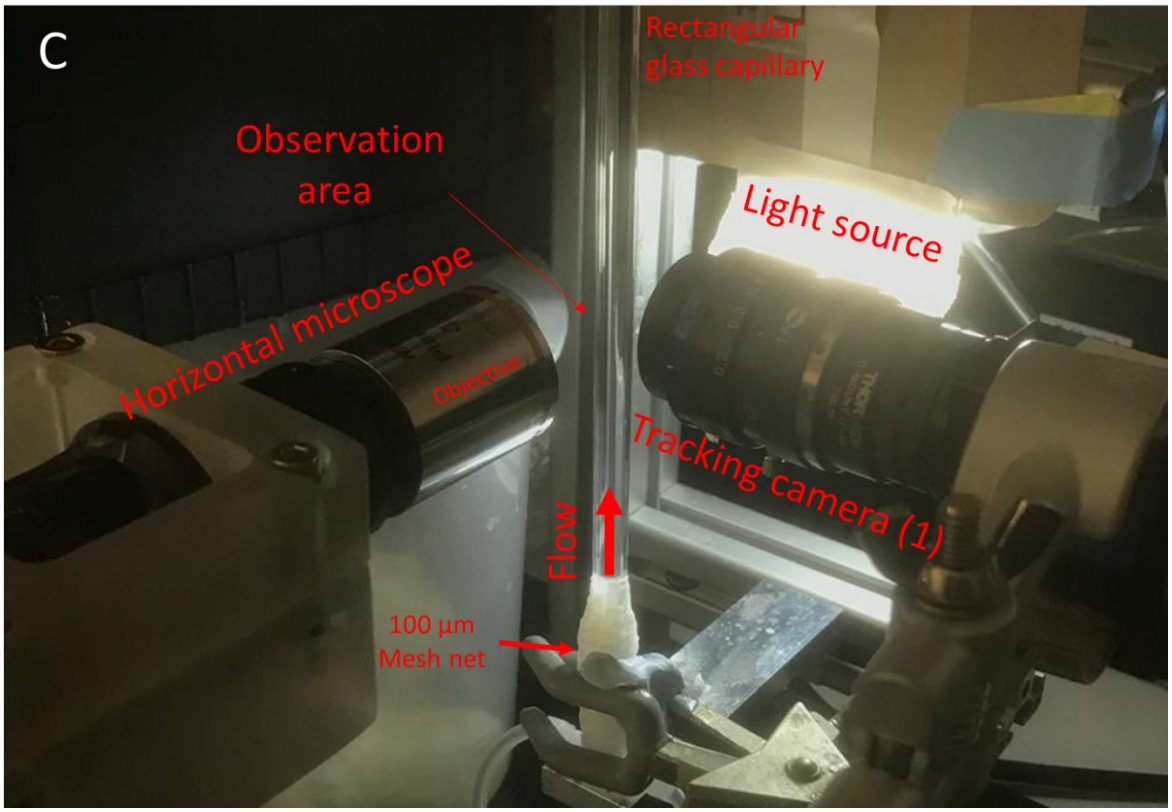
C
Rectangular
glass capillary
Observation
area
Light source
Horizontal microscope
Objective
Tracking camera (1)
Flow
100 µm
Mesh net

262
263

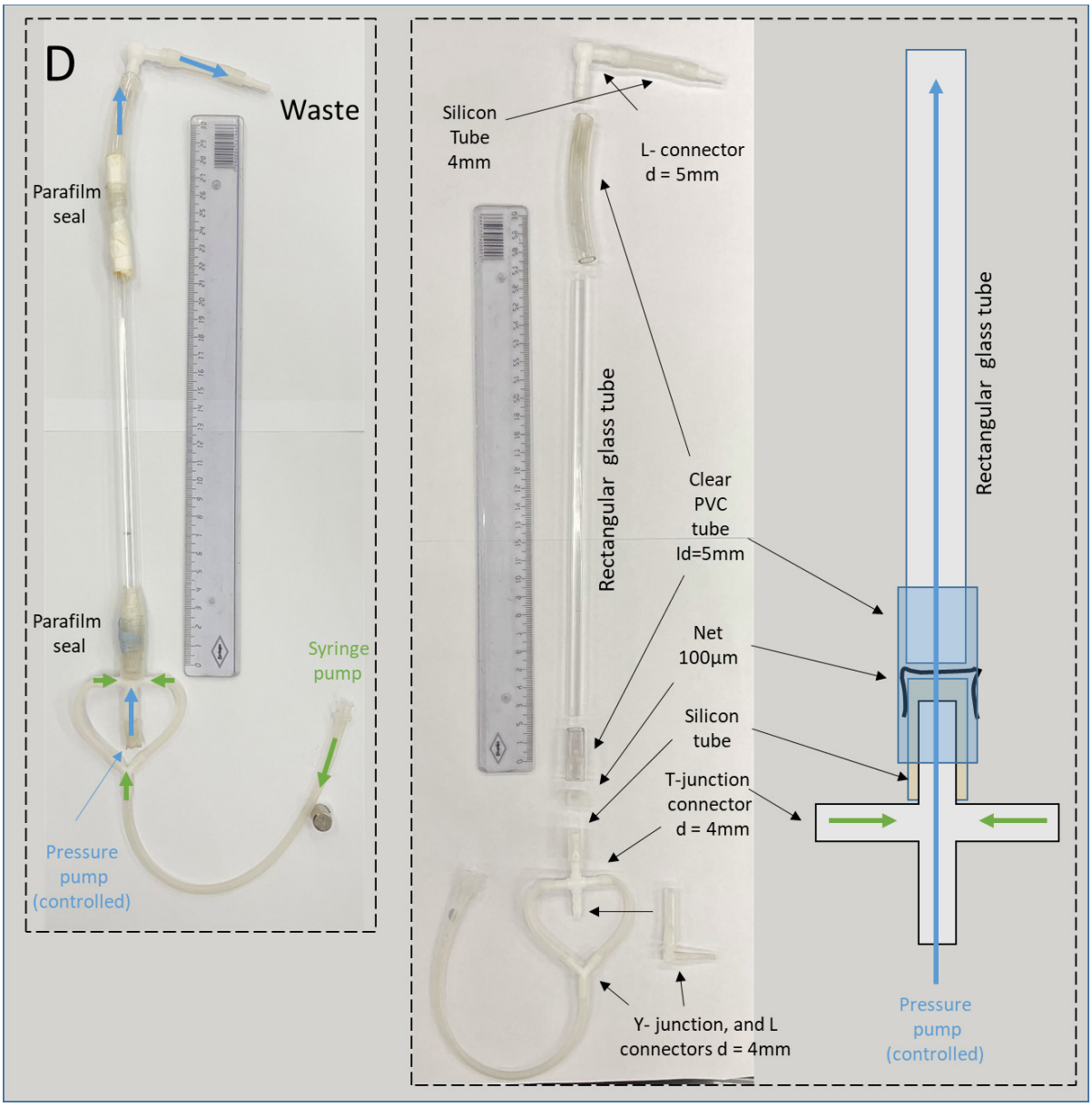

Fig. 1. Experimental setup of the 'endless-ocean-column' millifluidic device. (**A–D**) A pressure controller is used to apply pressure to an artificial seawater medium and push it through a flow meter and the column, a rectangular glass capillary of length 20 cm and 0.5 × 0.5 cm cross-section. By adjusting the flow rate to be equal to the sinking speed of a freely sinking marine particle within the column, the particle remains stationary in front of a lateral camera and a frontal vertical microscope. Images from the lateral camera are used to determine the vertical position of the suspended particle by image analysis, and the position and velocity of the particle are then used to control an air pump to set the flow feeding the column. At the same time, the frontal vertical microscope is used to image the suspended particle at high magnification (18×

magnification). Sinking speed is determined by the flow rate from the online flow meter. The particle is observed 8–10 cm above a 100 µm mesh net located at the bottom of the tube, sealed with parafilm (panels C and D). A syringe pump, connected via silicone tubing through a Y-shaped connector, feeds the T-junction at the base of the endless ocean tube. The syringe pump is used to manually adjust the flow, stabilizing and "trapping" the particle at the start of the experiment (depicted in green in panels A, B, and D). Once the experiment begins, this flow is deactivated, and an algorithm-controlled pressure pump supplies flow from below (depicted in blue in panels A, B, and D).

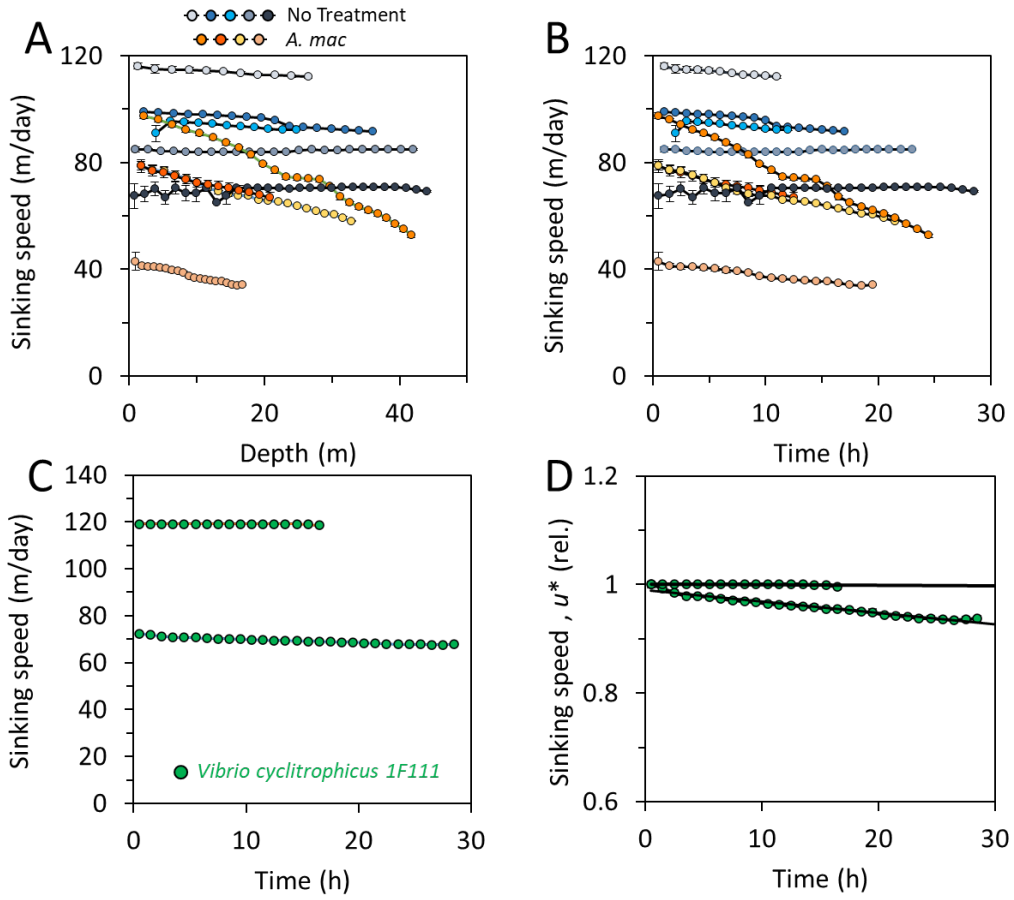

Fig. 2. Sinking speed of particles in the presence of a biofilm-forming or a free-living bacterial strain. (**A–D**) Particle sinking speed was measured in an 'endless-ocean-column' for up to 30 h in the presence of *Alteromonas macleodii* (**A** and **B**; orange, $n = 4$), in sterile artificial seawater (**A** and **B**; blue, $n = 5$), or in the presence of the non-biofilm free-living bacterial strain *Vibrio cyclitrophicus* 1F111 (**C** and **D**; green, $n = 2$). Sinking speed is presented as a function of depth (A) or time (B–D). Data in (A) and (B) are the raw data used to make Fig. 1, B and C, but are here presented as absolute values of sinking speed rather than relative. Values for V. *cyclitrophicus* 1F111 are presented as absolute speed (C) and relative speed (D). Note that in panel D, the average slope of sinking speed as a function of time for treatments using *V. cyclitrophicus* 1F111 (-0.1%/h) is similar to that of no bacterial treatment (-0.17%/h). Source data are provided as a Source Data file. The sinking speed values are presented as hourly averages. The bars represent the standard deviation calculated over the 1-hour interval.

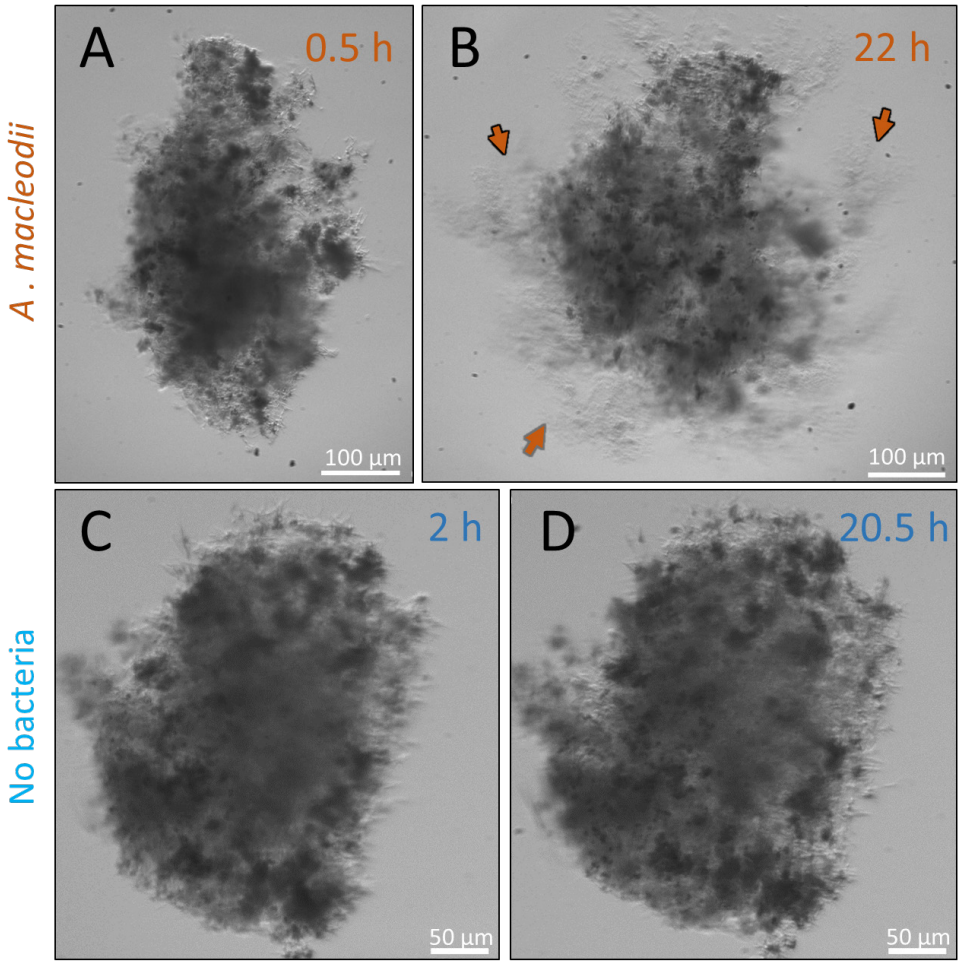

Fig. 3. Bacterial biofilm accumulates on sinking particles. Images of two examples of marine snow particles at two time points during a sinking experiment. (**A** and **B**) In the presence of *A. macleodii.* Orange arrows indicate bacterial biofilm that accumulated on the periphery of the particle after 22 h sinking. (**C** and **D**) In sterile artificial seawater. Pairs of images (A and B, C and D) are images of the same particle at different time points—upper right corners, time (h); lower right corners, scale bar (µm).

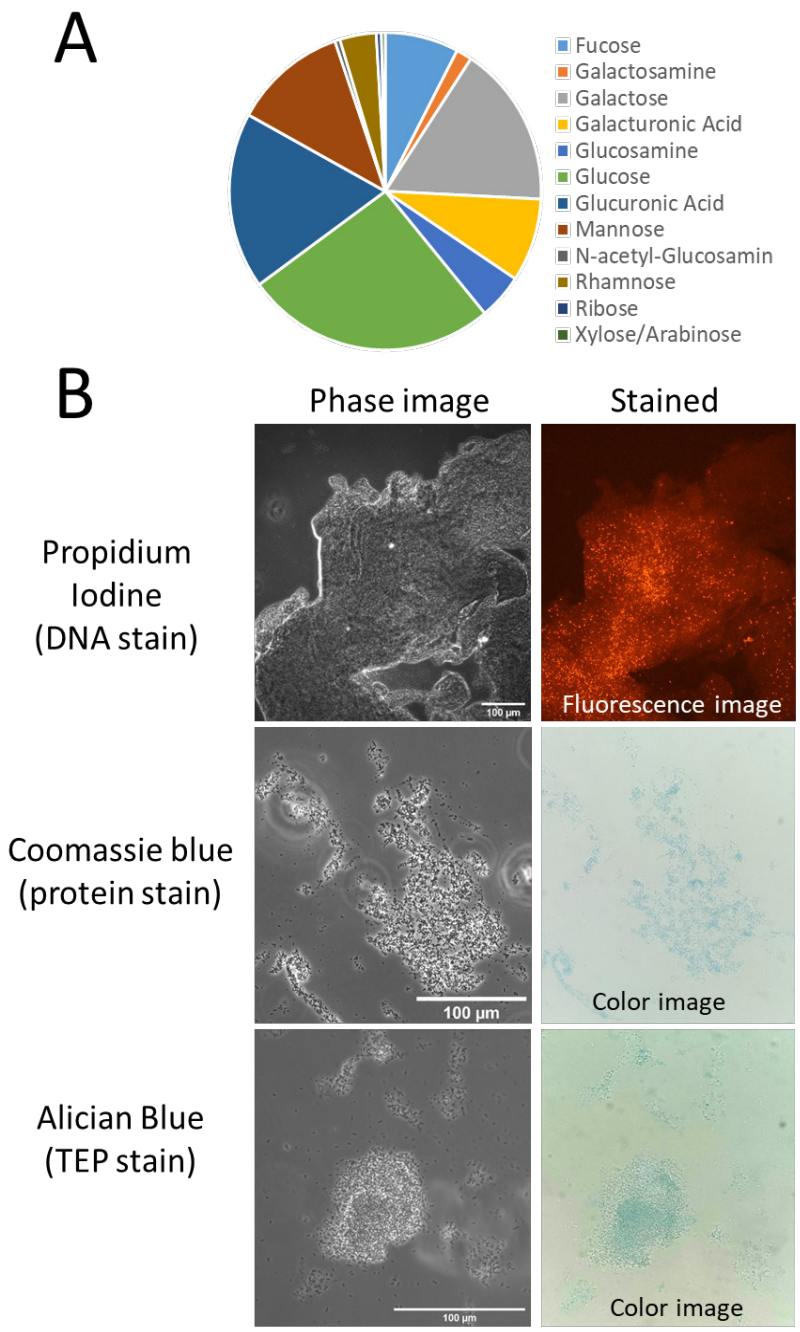

305

306 **Fig. 4. *A. macleodii* biofilm is composed of polysaccharides, eDNA and proteins.** (**A**) An
307 acid-based polysaccharide fragmentation analysis identifies the composition of *A. macleodii*
308 EPS. (**B**) Images of stained biofilm aggregates. Propidium iodine stain for DNA was detected by
309 fluorescence (excitation 587 nm, emission 610 nm). Coomassie blue, for protein, and Alician
310 blue, for TEP, were visualized using a digital camera (iPhone 13 mini) from the eyepiece hole of
311 the microscope. Scale bars 100 µm for all images. Source data are provided as a Source Data
312 file.

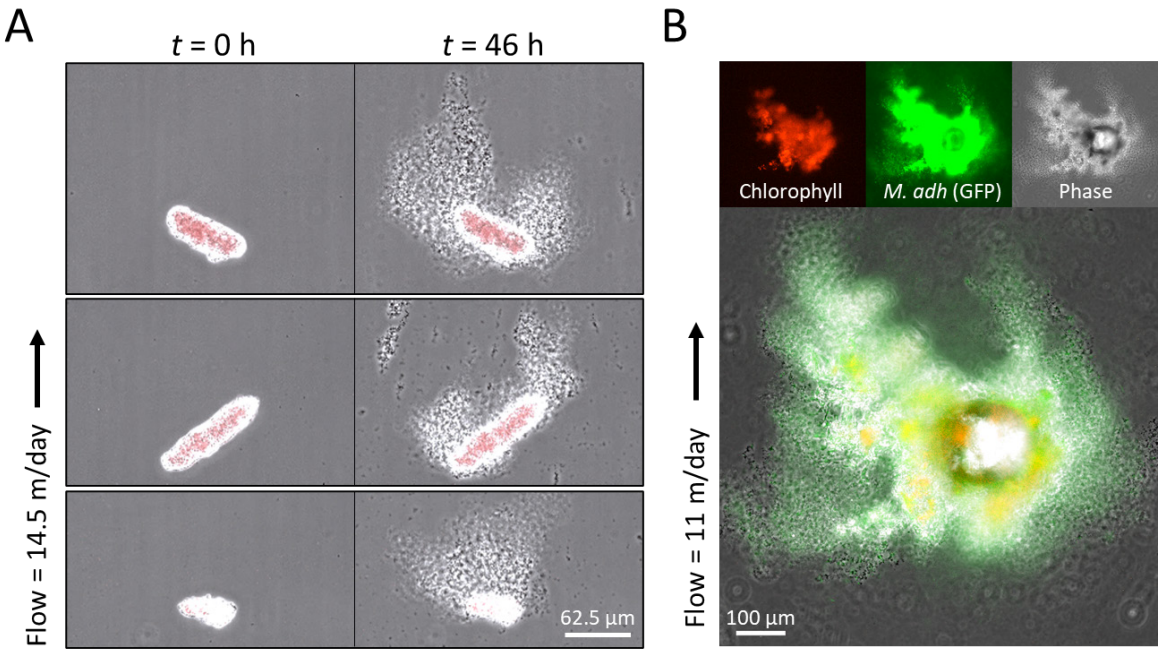

Fig. 5. Biofilm can also accumulate on copepod fecal pellets and serve as an attachment site for other marine bacteria. (**A**) Accumulation of biofilm on three copepod fecal pellets maintained in a microfluidic channel at a flow rate of 14.5 m/day. Images show two time points for each particle, $t = 0$ h (left) and $t = 46$ h (right). (**B**) Accumulation of GFP-tagged *Marinobacter adhaerens* on an algal particle maintained in a microfluidic channel in flow in the presence of *A. macleodii.* The image shows biofilm accumulation on the particle after 27 h at a flow rate of 11 m/day. Red, chlorophyll; green, GFP signal from *M. adhaerens;* gray, phase image; lower magnified image, three channels merged.

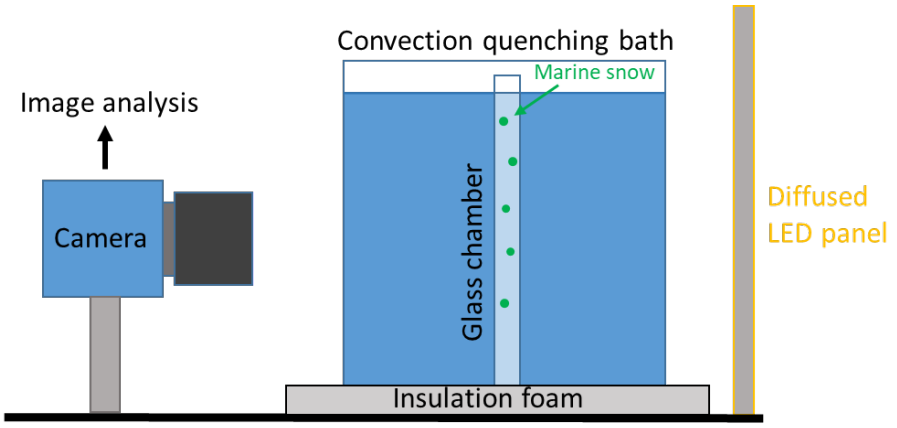

Fig. 6. Bulk sedimentation chamber. For bulk measurements of sinking speed, particles were imaged as they sank within a glass chamber (10 mm × 6 mm × 150 mm; VitroCom). To quench convective currents, we placed the chamber within a custom-made acrylic bath (140 mm × 140 mm × 140 mm). An LED panel with a built-in diffuser was placed behind the bath at a distance of 100 mm to provide homogeneous lighting. Imaging was performed at 5 Hz from a distance of 250 mm using a CMOS camera (SVS Vistek EXO) with a fixed focal lens (Myutron HF3514V-2). The glass chamber and quenching bath were filled with salt water (3.5% w/v) and left to equilibrate to room temperature for 90 min before each experiment.

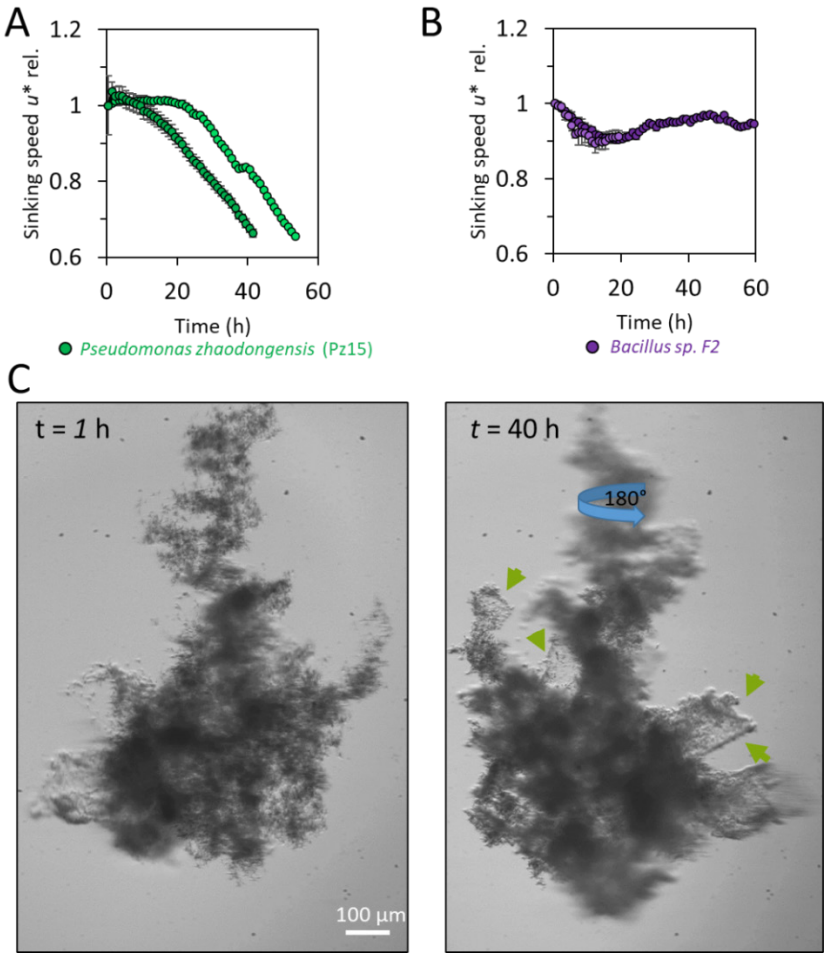

Fig. 7. Biofilm of other bacteria can also slow the sinking of particles, yet not all biofilm-forming bacteria can. (**A**–**B**) Two bacterial strains isolated from marine snow were tested for their ability to slow down the sinking of particles. Among the two, *Pseudomonas zhaodongensis* Pz15 (**A**) but not *Bacillus* sp. F2 (**B**) slowed down the sinking of the particle. The sinking speed values are presented as hourly averages. The bars represent the standard deviation calculated over the 1-hour interval. (**C**) Images of a marine snow particle at two time points (after 1 h, left and 40 h, right) during a sinking experiment in the presence of *Pseudomonas zhaodongensis* (Pz15). Green arrows indicate bacterial biofilm that accumulated on the periphery of the particle observed after 39 h sinking. Tendrils are less pronounced in experiments with this strain but deceleration is observed. This indicates that the density change induced by this biofilm is likely the dominant factor responsible for the deceleration. Alternatively, some of the biofilm of this strain that we see in the microfluidic experiment (**Supplementary Movie 3**) is not visualized well in the endless-ocean-column setup. Source data are provided as a Source Data file.

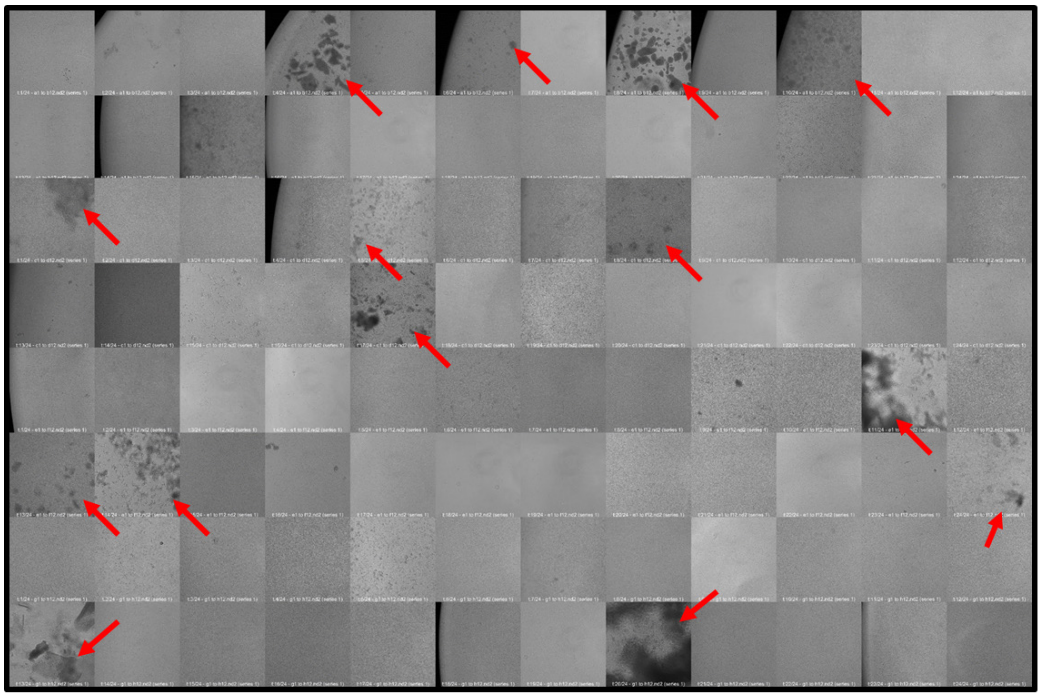

Fig. 8. A large proportion of bacteria isolated from natural marine snow can produce biofilm. A panel of 96 strains of bacteria that had been isolated from marine snow particles were tested for their ability to form biofilm when grown for two days in 2216 MB rich medium. About 10% (14/96) of the isolates formed visible biofilm (red arrow).

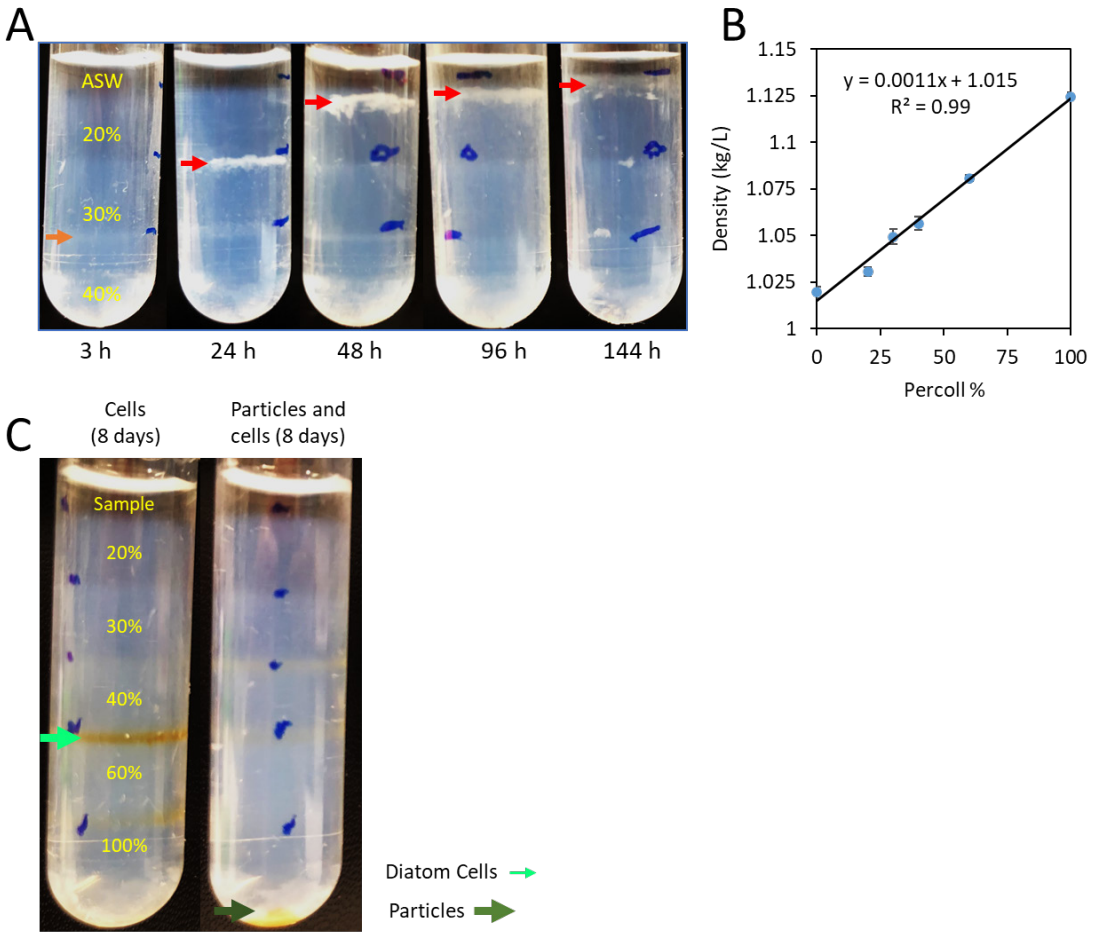

Fig. 9. Density of *A. macleodii* biofilm and of marine particles. (**A**) The density of *A. macleodii* biofilm (red arrows) and free-living *A. macleodii* bacteria (orange arrow) was measured using a Percoll gradient as the biofilm developed. Development of biofilm is observed from 24 h of *A. macleodii* growth onwards. Biofilm accumulates on the 30% layer of Percoll after 24 h and on the 20% layer after 48 h, whereas free bacteria settle to denser layers. (**B**) To convert from Percoll percentage to absolute density, a standard curve was made by measuring the density of each layer of Percoll and comparing its percentage with the weight of 1 ml volume of liquid. (**C**) Free-living *Phaeodactylum tricornutum* algae (8-day-old culture) accumulate mostly in the 40% Percoll layer (light green arrow). Small amounts of free-living algae are also found in other density layers, indicating a variable density within the algal population. After 8 days of aggregation in a rolling tube, the particles (dark green arrow) have a density greater than 100% Percoll, which corresponds to >1.125 kg/L (see **supplementary methods** for experimental procedure). Source data are provided as a Source Data file.

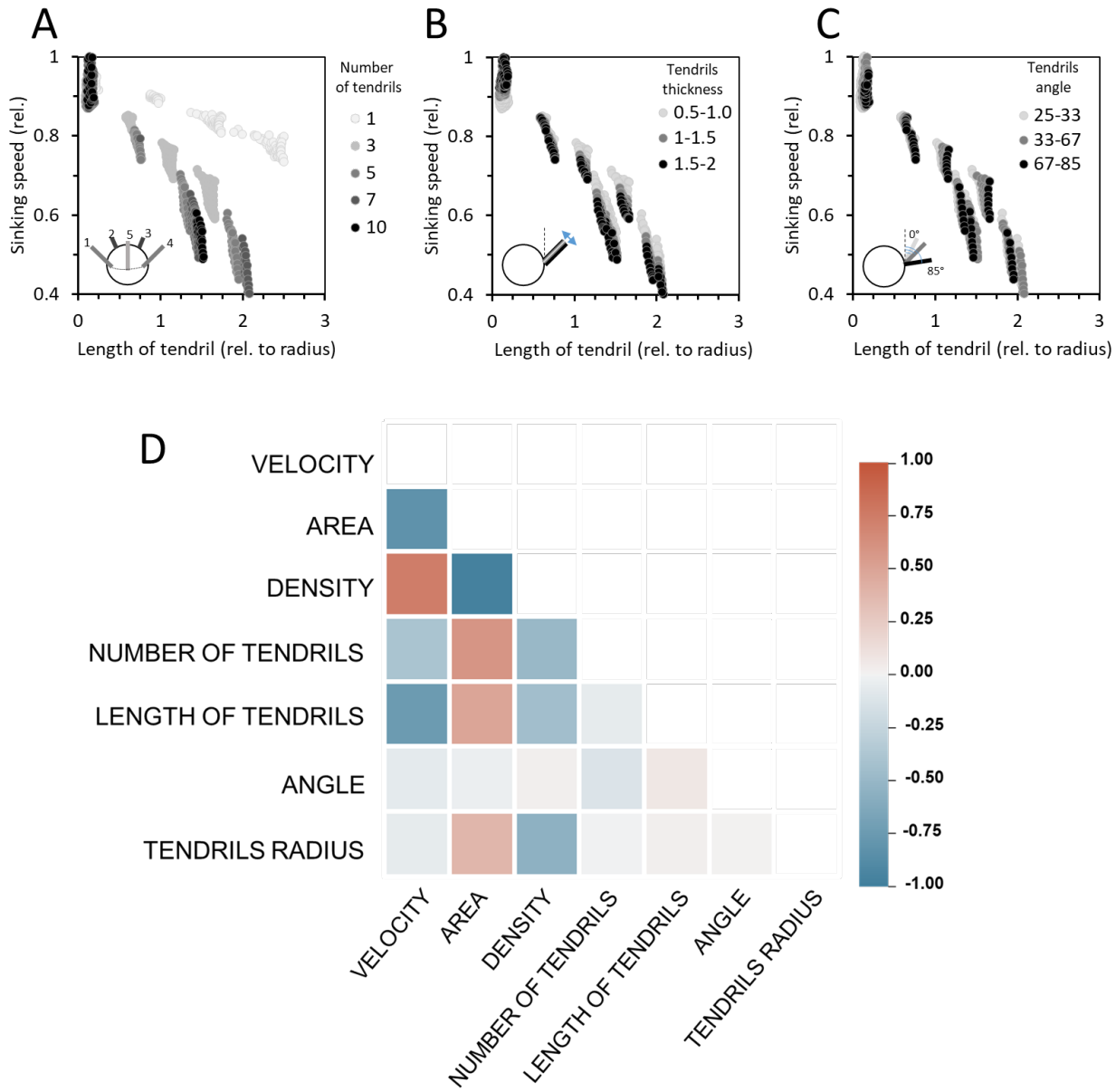

Fig. 10. Biofilm increases the drag on particles and, therefore, slows their sinking speed. Sensitivity analysis for the model of the sinking of spherical particles with tendrils. The three-dimensional numerical model was developed to test the effect of biofilm accumulation on particles, by coupling fluid flow simulations with an ordinary differential equation (ODE) to calculate the balance of forces acting on a solid object as it sinks. (**A**) Impact of the number of tendrils (grayscale) on the sinking of particles. Where the tendril angle ranges between 25° and 85° (relative to the angle of 12:00 o'clock), and the tendril radius (thickness) between 0.5 rt and 2 r_t; Note that the tendrils were placed in a radial symmetry around the horizontal circumference.

(**B**) Impact of the radius of the tendrils (grayscale) on the sinking of particles. Where the number of tendrils ranges between 3 and 10, and tendril angle between 25° and 85°. (**C**) Impact of the angle of the tendrils (grayscale) on the sinking of particles. Where the number of tendrils ranges between 3 and 10, and the tendril radius (thickness) between 0.5 r_t and 2 r_t. All cases represent the attachment of suspended biofilm with a density equivalent to that of water ($\rho_b = \rho_f$), similar to the case of *A. macleodii* biofilm tendrils. The factors tested in each panel are represented in the inset illustrations. (**D**) Correlation matrix of the model parameters. Correlation coefficients are color-coded, with positive correlations in red and negative correlations in blue. The matrix reveals a strong negative correlation between particle surface area, tendril length, and sinking velocity. As expected, particle density shows a positive correlation with sinking speed. The number and angle of the tendrils exhibit a weaker correlation with sinking speed, indicating a lesser impact of these parameters on the overall sinking speed. Source data are provided as a Source Data file.

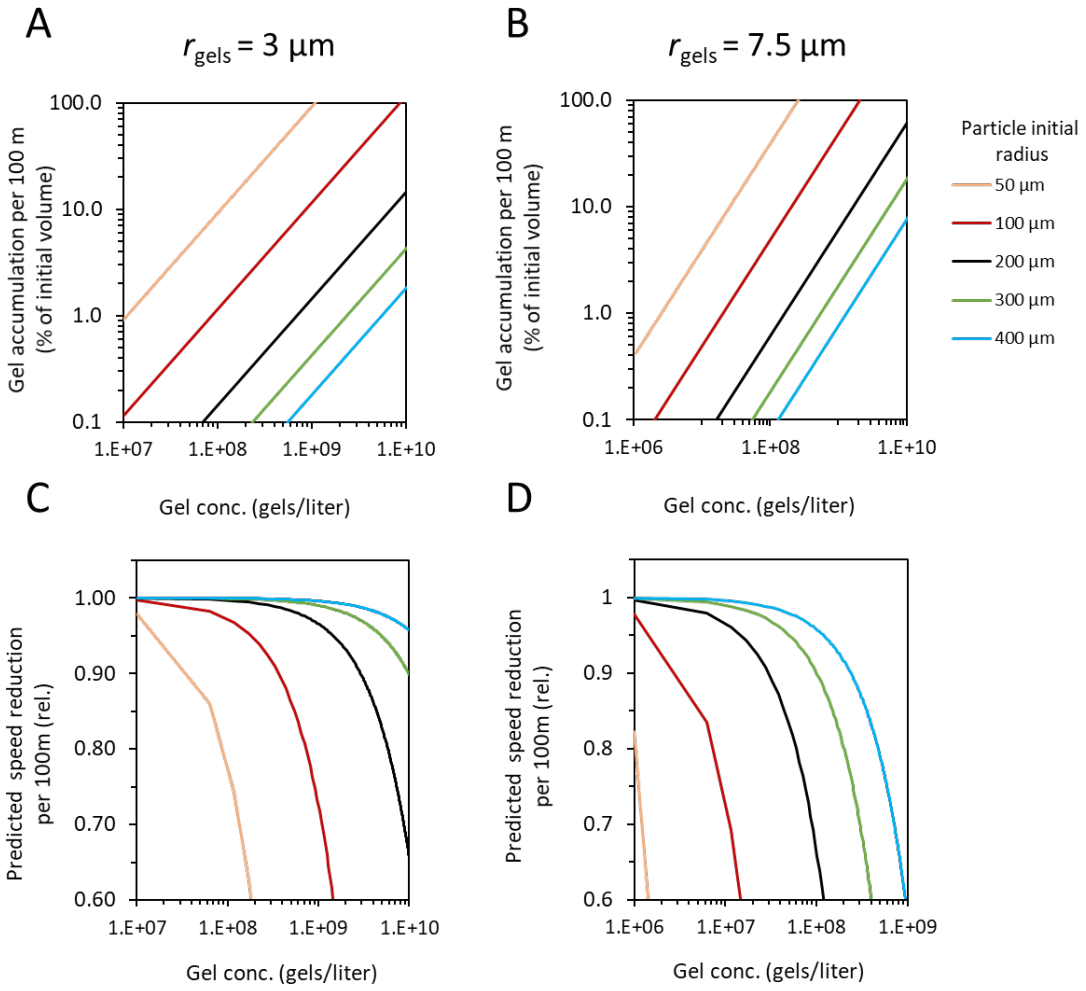

Fig. 11. Impact of biogel concentration on particle sinking speeds. (A and B) Influence of biogel concentration in the water column on the accumulation of gel on particles traversing 100 m through water. Results are independent of the particle sinking speed. Colors represent particles of different initial sizes (color legend on right). (C and D) Estimation of sinking reduction based on biogel volume addition, using two different scenarios (based on the numerical model). The calculation incorporates the addition of biogel in the form of tendrils. Biogel aggregates are assumed to have a radius of 3 µm (A and C) or 7.5 µm (B and D). Source data are provided as a Source Data file.

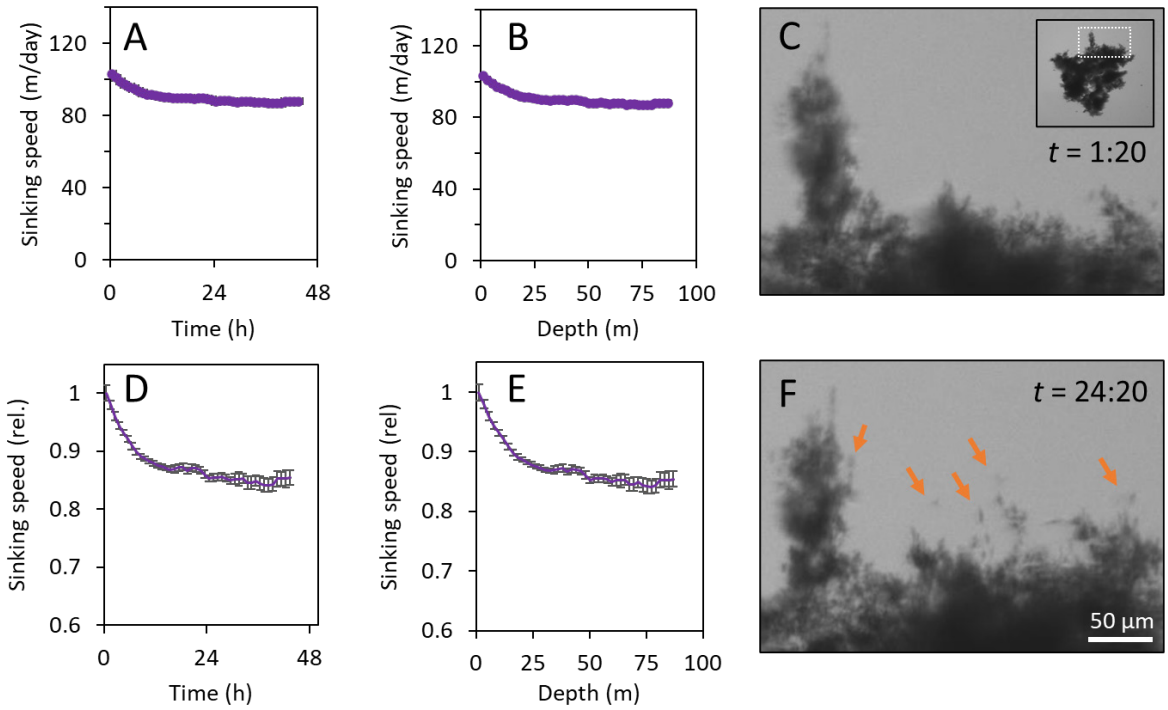

Fig. 12. In the absence of accumulation of biofilm, biofilm growth alone leads to relatively little reduction in sinking speed of particles in our experimental system. (A, B, D, and E) The sinking speed of a particle pre-colonized by *A. macleodii* and sinking in sterile seawater as a function of time, for absolute speed (**A**) and speed relative to the initial speed (**D**), and as a function of equivalent depth, for absolute speed (**B**) and relative speed (**E**). The sinking speed values are presented as hourly averages. The bars represent the standard deviation calculated over the 1-hour interval. (**C** and **F**) Images of the top of a particle (inset in C). Small amount of biofilm has developed about 24 h post inoculation (orange arrows in (F) relative to the same area on the particle at time 1:20 h (C)). The biofilm on the particle, in this case, is purely a result of growth, as no *A. macleodii* biofilm was present in the ASW reservoir feeding the endless ocean column. Source data are provided as a Source Data file.

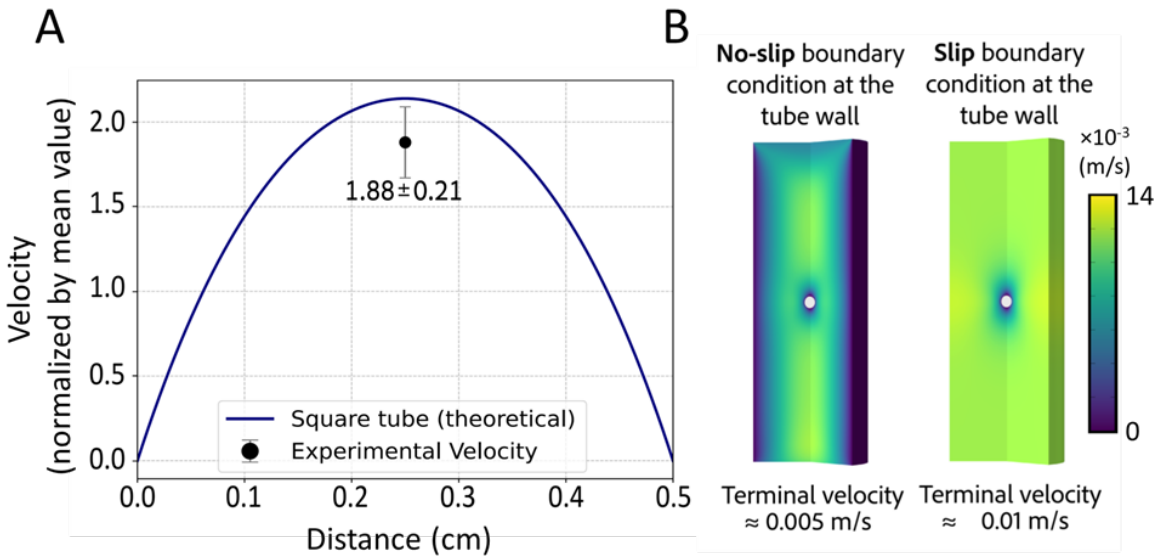

Fig 13. The flow velocity inside the experimental column, normalized by its mean value. (**A**) The solid line is the theoretical velocity profile within a square tube with a side length of 0.5 cm (e.g., Delplace 2018) [22]. The velocity at the center of the tube is 2.13 times the mean velocity. The black circle indicates the experimentally determined mean value of the ratio between the measured sinking velocity and the average flow velocity, which was 1.88. The bar represents the standard deviation calculated from 10 replicates (±0.21). **(B)** Three-dimensional numerical model of a spherical particle sinking in the column in the presence of counter-flow, solved using COMSOL. The model calculates the mean velocity of the counter-flow required to keep the particle stationary. The colorbar represents the magnitude of the fluid velocity. This model evaluates the influence of the tube walls on fluid flow and, consequently, on the particle's terminal velocity. When a no-slip boundary condition is imposed at the tube walls (left panel), the flow velocity required to balance the particle's sinking is approximately half that of a system with slip boundaries (right panel). This further confirms that the ratio between the particle sinking speed and the mean flow velocity in the experimental column (which has no-slip boundaries) is approximately 2, aligning with the theoretical and experimental results (panel A).

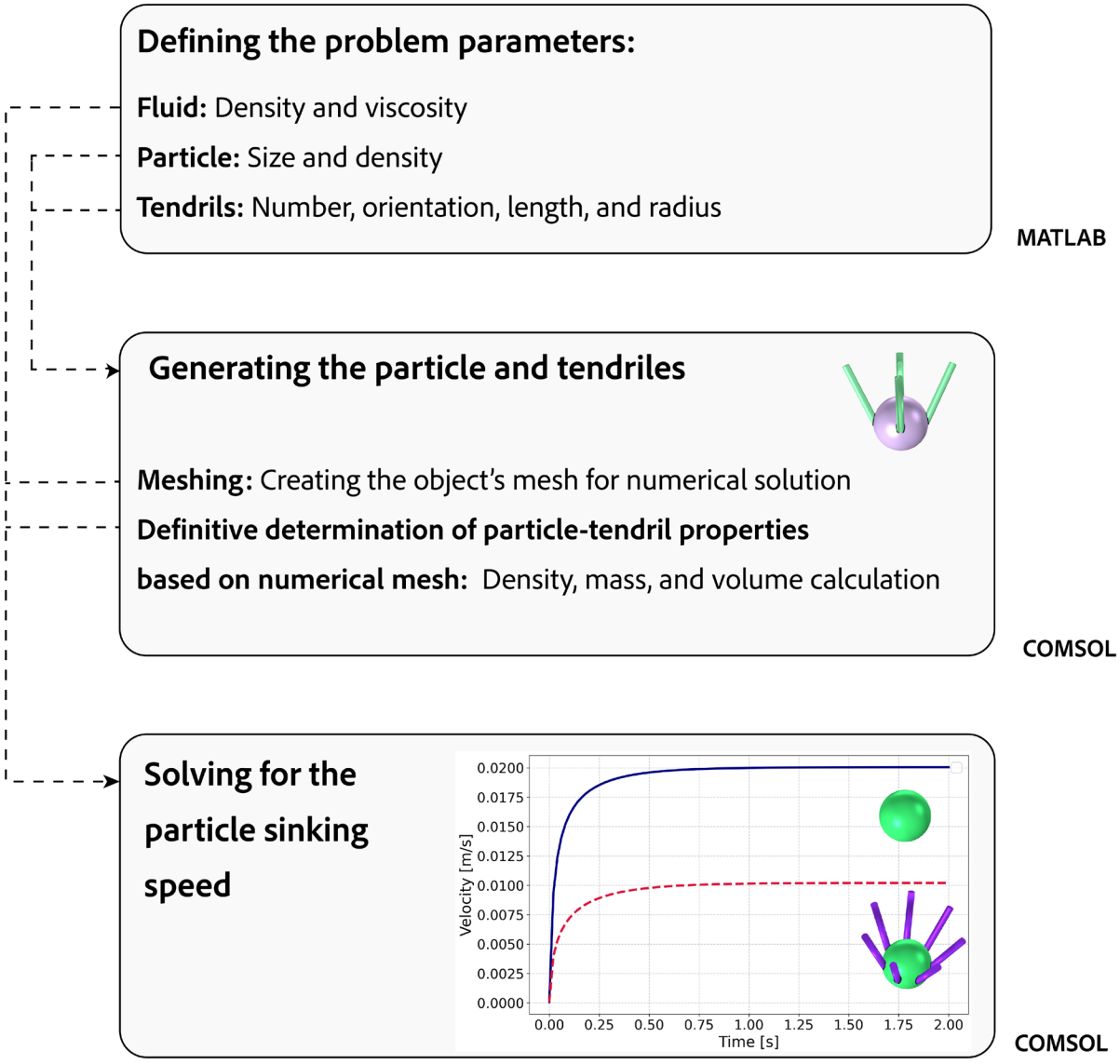

Fig 14: Workflow for calculating the sinking velocity of particles with tendrils using the LiveLink MATLAB-COMSOL interface. The process begins in MATLAB with the definition of problem parameters, including fluid properties (density and viscosity), particle characteristics (size and density), and tendril attributes (number, orientation, length, and radius) (upper panel). These parameters are then transferred to COMSOL, where MATLAB executes the first COMSOL model to generate the geometry of the composite object, consisting of the particle and tendrils (middle panel). Due to the discretization involved in meshing, the resulting composite object may exhibit slight deviations from the analytically defined properties. Therefore, COMSOL recalculates definitive properties such as density, mass, and volume based on the

meshed object. The adjusted properties are then passed back to MATLAB, which subsequently executes the second COMSOL model to solve Equations 1–4 and determine the sinking velocity (bottom panel). The image in the bottom panel compares the sinking velocity of a particle with tendrils to that of a particle without tendrils. The *x*-axis in the bottom panel represents the time required for the particle to reach its terminal sinking speed.

Supplementary References

1. Alcolombri, U. *et al.* Sinking enhances the degradation of organic particles by marine bacteria. *Nat Geosci* **14**, 775–780 (2021).
2. Słomka, J. *et al.* Encounter rates prime interactions between microorganisms. *Interface Focus* **13**, (2023).
3. Nguyen, T. T. H. *et al.* Microbes contribute to setting the ocean carbon flux by altering the fate of sinking particulates. *Nat Commun* **13**, 1657 (2022).
4. Bar-Zeev, E., Berman-Frank, I., Girshevitz, O. & Berman, T. Revised paradigm of aquatic biofilm formation facilitated by microgel transparent exopolymer particles. *Proc Natl Acad Sci U S A* **109**, (2012).
5. Passow, U. & Alldredge, A. L. Distribution, size and bacterial colonization of transparent exopolymer particles (TEP) in the ocean. *Mar Ecol Prog Ser* **113**, (1994).
6. Chajwa, R., Flaum, E., Bidle, K. D., Van Mooy, B. & Prakash, M. Hidden comet tails of marine snow impede ocean-based carbon sequestration. *Science (1979)* **386**, (2024).
7. Pedler, B. E., Aluwihare, L. I. & Azam, F. Single bacterial strain capable of significant contribution to carbon cycling in the surface ocean. *Proc Natl Acad Sci U S A* **111**, 7202–7 (2014).
8. White, A. R., Jalali, M., Boufadel, M. C. & Sheng, J. Bacteria forming drag-increasing streamers on a drop implicates complementary fates of rising deep-sea oil droplets. *Sci Rep* **10**, 1–14 (2020).
9. White, A. R., Jalali, M. & Sheng, J. Hydrodynamics of a Rising Oil Droplet With Bacterial Extracellular Polymeric Substance (EPS) Streamers Using a Microfluidic Microcosm. *Front Mar Sci* **7**, 1–14 (2020).
10. White, A. R., Jalali, M. & Sheng, J. A new ecology-on-a-chip microfluidic platform to study interactions of microbes with a rising oil droplet. *Sci Rep* **9**, 1–11 (2019).
11. Flemming, H. & Wingender, J. The biofilm matrix. *Nat Rev Microbiol* **8**, 623–33 (2010).
12. Lee, S. H., Secchi, E. & Kang, P. K. Rapid formation of bioaggregates and morphology transition to biofilm streamers induced by pore-throat flows. *Proceedings of the National Academy of Sciences* **120**, e2204466120 (2023).
13. Stoodley, P., Cargo, R., Rupp, C. J., Wilson, S. & Klapper, I. Biofilm material properties as related to shear-induced deformation and detachment phenomena. *J Ind Microbiol Biotechnol* **29**, 361–367 (2002).
14. Das, S. & Kumar, A. Formation and post-formation dynamics of bacterial biofilm streamers as highly viscous liquid jets. *Sci Rep* **4**, 7126 (2014).
15. Rusconi, R., Lecuyer, S., Guglielmini, L. & Stone, H. A. Laminar flow around corners triggers the formation of biofilm streamers. *J R Soc Interface* **7**, 1293–1299 (2010).
16. Hassanpourfard, M. *et al.* Bacterial floc mediated rapid streamer formation in creeping flows. *Sci Rep* **5**, 130070 (2015).
17. Drescher, K., Shen, Y., Bassler, B. L. & Stone, H. A. Biofilm streamers cause catastrophic disruption of flow with consequences for environmental and medical systems. *Proc Natl Acad Sci U S A* **110**, 4345–50 (2013).
18. Robertson, J. M. *et al.* Marine bacteria Alteromonas spp. require UDP-glucose-4epimerase for aggregation and production of sticky exopolymer. *mBio* **15**, (2024).
19. Casillo, A., Lanzetta, R., Parrilli, M. & Corsaro, M. M. Exopolysaccharides from marine and marine extremophilic bacteria: Structures, properties, ecological roles and

applications. *Marine Drugs* vol. 16 Preprint at https://doi.org/10.3390/md16020069 (2018).
20. Sampaio, I. C. F. *et al.* Composition of Xanthan gum produced by Xanthomonas campestris using produced water from a carbonated oil field through Raman spectroscopy. *J Photochem Photobiol B* **213**, 112052 (2020).
21. Gralka, M., Pollak, S. & Cordero, O. X. Genome content predicts the carbon catabolic preferences of heterotrophic bacteria. *Nat Microbiol* **8**, 1799–1808 (2023).
22. Delplace, F. Laminar flow of Newtonian liquids in ducts of rectangular cross-section a model for both physics and mathematics. *Open Access Journal of Mathematical and Theoretical Physics* **1**, 198–201 (2018).